

Temporal structure of blobs in NSTX

Cite as: Phys. Plasmas **29**, 072504 (2022); <https://doi.org/10.1063/5.0097282>

Submitted: 27 April 2022 • Accepted: 30 June 2022 • Published Online: 21 July 2022

 S. J. Zweben,  M. Lampert and  J. R. Myra



[View Online](#)



[Export Citation](#)



[CrossMark](#)



Physics of Plasmas
Features in Plasma Physics Webinars

Register Today!

Temporal structure of blobs in NSTX

Cite as: Phys. Plasmas **29**, 072504 (2022); doi: 10.1063/5.0097282

Submitted: 27 April 2022 · Accepted: 30 June 2022 ·

Published Online: 21 July 2022



View Online



Export Citation



CrossMark

S. J. Zweben,^{1,a)} M. Lampert,¹ and J. R. Myra²

AFFILIATIONS

¹Princeton Plasma Physics Laboratory, Princeton, New Jersey 08540, USA

²Lodestar Research Corporation, Boulder, Colorado 80301, USA

^{a)}Author to whom correspondence should be addressed: stewart.zweben@gmail.com

ABSTRACT

The time dependence of the blob pulse shape and the waiting time between blobs was found using data from the gas puff imaging diagnostic in NSTX. The database used was of 103 shots from 2010 as described in a previous paper (Zweben *et al.*, Phys. Plasmas **29**, 012505 (2022)). The blob pulse shape was well fit by an exponential rise and fall where the average rise time was $\tau_r = 9.0 \pm 2.7 \mu\text{s}$ and the average fall time was $\tau_f = 16.6 \pm 5.8 \mu\text{s}$. The waiting times between blob pulses above a threshold of three times the mean had a broad distribution with an average of $\tau_w = 1.2 \pm 0.85 \text{ ms}$ over the database. The blob intermittency parameter $\gamma_b = \tau_d/\tau_w$, where the blob pulse duration was $\tau_d = \tau_r + \tau_f$, ranged from $\gamma_b \sim 1\%$ to 5% for shots in this database and increased almost linearly with the blob fraction.

Published under an exclusive license by AIP Publishing. <https://doi.org/10.1063/5.0097282>

I. INTRODUCTION

The present short paper was motivated by recent measurements of the blob fraction in NSTX,¹ in which a theoretical model was presented relating the measured blob fraction to a statistical theory of blob pulses.² An assumption of that model was that tokamak blob pulses have an exponential pulse shape and a randomly distributed waiting time between blobs. Here, we present an analysis of the temporal structure of blobs in NSTX to test those assumptions, using the same database of gas puff imaging (GPI) data discussed in Ref. 1. Such a time-dependent blob pulse analysis was not done before for NSTX GPI data.

There have been several previous experimental and theoretical studies of the time dependence of blob pulse shapes in the scrape-off layer (SOL) of tokamaks (“blobs” are sometimes called “intermittent fluctuations” or “edge filaments”). Early experimental studies were done with Langmuir probe measurements in DIII-D,³ and the connection between experiments and theory was reviewed in 2011.⁴ For example, blob pulse arrivals measured using GPI in Alcator C-Mod were shown to follow a homogeneous Poisson process,⁵ and a recent study on the same device gave a detailed comparison between the statistics of SOL fluctuations measured by a mirror Langmuir probe (MLP) and GPI.⁶

Understanding the statistical properties of blobs in the SOL is important for several reasons. The interaction of plasma with neutrals (e.g., ionization) and material surfaces is, in general, nonlinear; therefore, in some cases, an analysis using a statistical distribution of small and large amplitude events may be more appropriate than employing

mean plasma parameters. On the other hand, when a mean-field analysis is sufficient, previous theoretical work^{7,8} has shown that blob statistics can be used to provide a framework for calculating the blob contribution to mean SOL profiles, linking statistical properties to dynamical properties such as blob velocity and lifetime. These interrelationships provide a motivation for examining the statistics of blobs detected by the GPI diagnostic in NSTX.

The NSTX GPI diagnostic was described in Ref. 1 and GPI was reviewed in Ref. 9. A fast camera (Vision Research Phantom 710) views a deuterium neutral gas cloud puffed into the edge plasma near the outer midplane separatrix using a D α filter to image a neutral deuterium emission line during the steady-state part of the discharge. The camera-viewing angle is as near as possible aligned along the local magnetic field, which is tilted at an angle of about 36° with respect to the toroidal direction in NSTX, resulting in images of the local D α light emission from the cloud which are approximately radial (i.e., perpendicular to the local separatrix) vs poloidal or “binormal” (i.e., along the local separatrix). The camera images all have 64 × 80 pixels taken at 400 000 frames/s (2.5 $\mu\text{s}/\text{frame}$). The GPI camera in NSTX views an area of about 24 cm radially by 30 cm poloidally, i.e., normal and binormal to the local magnetic field and centered near the separatrix just above the outer midplane. The raw image data are averaged over ± 1 pixel or 1.1 cm in each direction at each time to reduce noise, which is consistent with the optical resolution of the GPI diagnostic of $\sim 1 \text{ cm}$.¹

For the present paper, the GPI blob pulse data for each shot are analyzed for a representative sample of six pixels in a radial array at

the poloidal center of the image (row No. 40 out of 80 rows). The radial range of these pixels is from 0 to 7.5 cm outside the local separatrix, which is the same radial range used in Ref. 1 to measure the blob fraction f_b , which was defined there as the fraction of time that the normalized GPI signal exceeded three times its time-averaged value, i.e., $f_b = \text{time}(\geq 3)/\text{time}(0)$, where $\text{time}(\geq 3)$ is the time when the normalized signal is ≥ 3 in a given pixel, and $\text{time}(0)$ is the total time of interest. The poloidal range used for measuring the blob fraction in the previous paper was ± 11.5 cm, i.e., row Nos. 10–69.

These GPI data are analyzed for a 10 ms period near the peak time of the GPI gas puff during which time the discharge is stationary and the GPI signal and signal/noise level are largest. The data are normalized by the time average for each pixel over this period, exactly as described in Ref. 1. The present analysis is done using the $D\alpha$ light emission itself with no attempt to unfold the underlying electron density, temperature, or possible neutral density fluctuations.

II. BLOB ANALYSIS RESULTS

Figure 1 shows a sample time series of the normalized GPI signal for three of these six pixels for 4 ms of an Ohmic shot No. 138121, the plasma parameters for which were shown in Table 1 of the previous paper.¹ The signal in Fig. 1(a) is from a pixel located 1.5 cm outside the separatrix. The average of this normalized signal is 1.0 on this scale (black horizontal line), and the blob threshold level is 3.0 on this scale (orange horizontal line). The signals in Figs. 1(b) and 1(c) are from the same shot, time, and row, but at pixels 4.5 and 7.5 cm outside the separatrix.

The blob pulses identified in the time segment of Fig. 1(a) are shown by shaded orange boxes. The height of each box is located at the local signal maxima, and the duration of each box is fixed at $\pm 50 \mu\text{s}$ (± 20 frames) around this maximum. Within this duration around each blob, no additional blobs are identified to avoid counting overlapping blobs (this process is started from the largest blob).

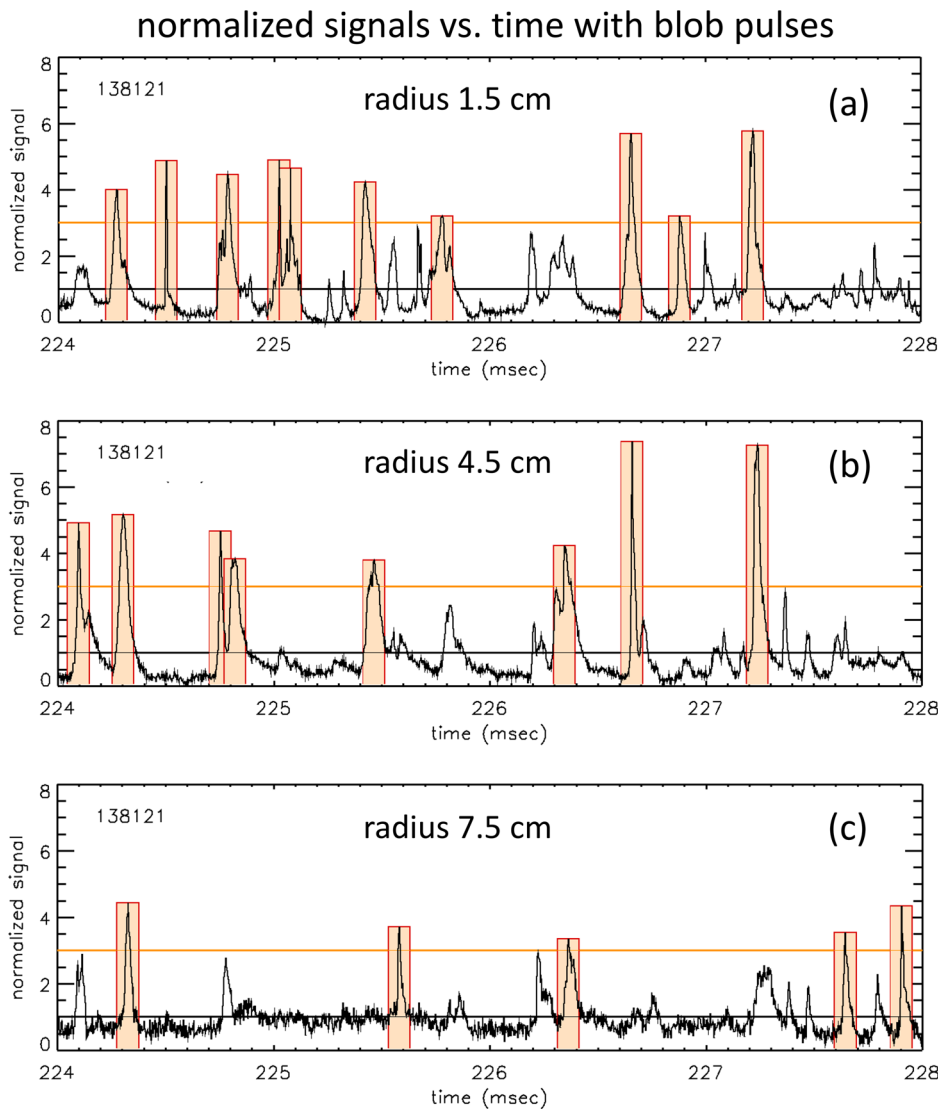


FIG. 1. Typical blob pulses over 4 ms around the peak time of the GPI signal for an Ohmic shot with a large blob fraction (No. 138121). In (a) is the normalized GPI signal from a single pixel at 1.5 cm outside the separatrix, and in (b) and (c) are single pixels at 4.5 and 7.5 cm outside the separatrix for the same shot, row, and time. The blob pulses are identified by the orange boxes around peak times when the normalized signals exceed the blob threshold of 3.0. The blob pulse boxes all have a $\pm 50 \mu\text{s}$ width around the local maxima, within which further blob maxima are not counted to avoid overlap; however, the $\pm 50 \mu\text{s}$ boxes occasionally overlap at 225 ms in (a).

There are 10 blobs identified within this 4 ms interval at 1.5 cm (a), eight blobs at 4.5 cm in (b), and six blobs at 7.5 cm in (c). There is an occasional overlap of these blob boxes in time, as shown at 225 ms in Fig. 1(a), but this is not a dominant effect in this analysis (as discussed further below).

Figure 2(a) shows the average blob pulse shape vs time at various radii for this same shot, averaged over 10 ms during the peak GPI signal time. Each curve is the average over 14–26 blobs in the single pixel at this radius and image row, as specified in the legend at the top right. The average normalized blob amplitude for these radii is in the range of 3.6–5.2, with the smallest normalized blob amplitudes at a radius of 0.0 cm. Since these averaged signal levels fall to near 1.0 at $\pm 50 \mu\text{s}$ around the peak of the blob pulses, there is not on average a significant overlap of blobs in time in this shot. Since this shot has nearly the largest blob fraction among this database,¹ blob overlap is also not a significant problem for the larger database.

Note that the blob pulses vs time for the six radii in Fig. 2(a) are not all-seeing entirely different blobs since the radial correlation length of blobs is typically larger than 1.5 cm and since they propagate radially. For example, the cross-correlation coefficient between the (10 ms long) signals at 1.5 and 4.5 cm has a maximum of 0.55 at a time delay of $17.5 \mu\text{s}$, and the cross-correlation coefficient between 1.5 and 7.5 cm has a maximum of 0.35 at a time delay of $37.5 \mu\text{s}$. Thus, some of these pixels are seeing different parts of the same blob at different space and time locations. However, the time dependence of the blob pulse shape as shown by the black curve with data points in Fig. 2(b) should be considered an average over space in the SOL, and so, each radial (or poloidal) pixel contains data equally relevant for this average blob pulse shape.

The radially averaged blob pulse amplitude vs time in Fig. 2(b) was fit separately for its rise and fall times using exponential shapes between the peak value at 0 ms and the in-between-blob level of almost 1.0 at $\pm 50 \mu\text{s}$. For example, the fits for the fall time τ_f were of the form:

$\text{fit} = (\text{peak} - 1.0) \exp(-t/\tau_f) + 1.0$. The best (least-squared) fits were found with respect to the data to the nearest $1 \mu\text{s}$ using the 21 time points from 0 to $+50 \mu\text{s}$ for the fall time and the 21 time points from 0 to $-50 \mu\text{s}$ for the rise time, as shown by the orange lines. For this shot, the rise time was the best fit by $\tau_r = 10 \mu\text{s}$ and the fall time by $\tau_f = 17 \mu\text{s}$.

The quality of these fits can be assessed by the standard deviations of the exponential fits from the average blob data points in Fig. 2(b). These standard deviations have a clear minimum at the best fit times to well within $\pm 2 \mu\text{s}$, as shown in the inset in Fig. 2(b). For example, the standard deviation is 0.16 (in normalized blob amplitude units) for the best rise time fit of $10 \mu\text{s}$, compared to 0.23 for an assumed $8 \mu\text{s}$ rise time and 0.24 for a $12 \mu\text{s}$ rise time. Similarly, the best fall time fit of $17 \mu\text{s}$ has a standard deviation of 0.08 compared to 0.12 for an assumed $15 \mu\text{s}$ fall time and 0.16 for $19 \mu\text{s}$. Thus, the uncertainties in the rise or fall time fits are less than $\pm 2 \mu\text{s}$ for this shot. Without the spatial averaging of ± 1 pixel used to reduce noise in this analysis, the average blob pulse amplitude increases slightly from 4.66 to 4.71 in this shot, and the average blob rise time decreases slightly from 10 to $9 \mu\text{s}$ and the fall time decreases from 17 to $16 \mu\text{s}$.

The same analysis which went into the Ohmic shot in Fig. 2(b) was repeated for the full 103 shot database of the previous paper.¹ Statistical results from this analysis are shown in Fig. 3, where 101 of these shots had a range of $N_b = 11$ –130 blobs per shot, including shot No. 138121 with $N_b = 109$ in Fig. 2(b). The two missing shots not shown in Fig. 3 had zero blobs in this analysis. Thirty of these 101 shots were Ohmic [no neutral beam injection (NBI) heating], 15 were in L-mode with low NBI heating power ($< 1.8 \text{ MW}$), and the rest were in H-mode with higher NBI power.

Figure 3(a) shows a comparison between the number of blobs N_b found in the blob pulse analysis described above vs the blob fraction “ f_b ,” as analyzed in the previous paper.¹ These blob fractions ranged from $f_b = 0.12\%$ – 4.84% over the 103-shot database when averaged

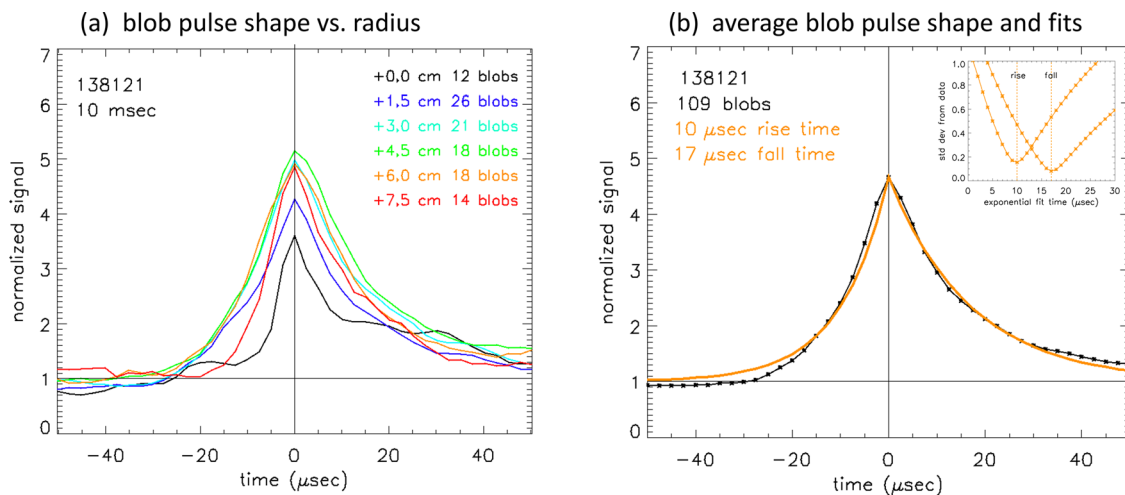


FIG. 2. In (a) are the time averages of the normalized GPI pulse shapes for six pixels over 10 ms at various radii for the row, shot, and times of Fig. 1 (No. 138121). The blob pulse shapes are shown from 0.0 to 7.5 cm outside the separatrix with the number of blob events shown in the legend and have a similar time dependence from 1.5 to 7.5 cm. In (b) is the average blob pulse shape over all 6 radii comprising a total of $N_b = 109$ blobs. This average shape is fit by the exponential curves shown in orange, with a rise time of $\tau_r = 10 \mu\text{s}$ and a fall time of $\tau_f = 17 \mu\text{s}$ for this shot (both to the nearest μs). The inset in (b) shows the standard deviations of the fits vs the assumed rise and fall times.

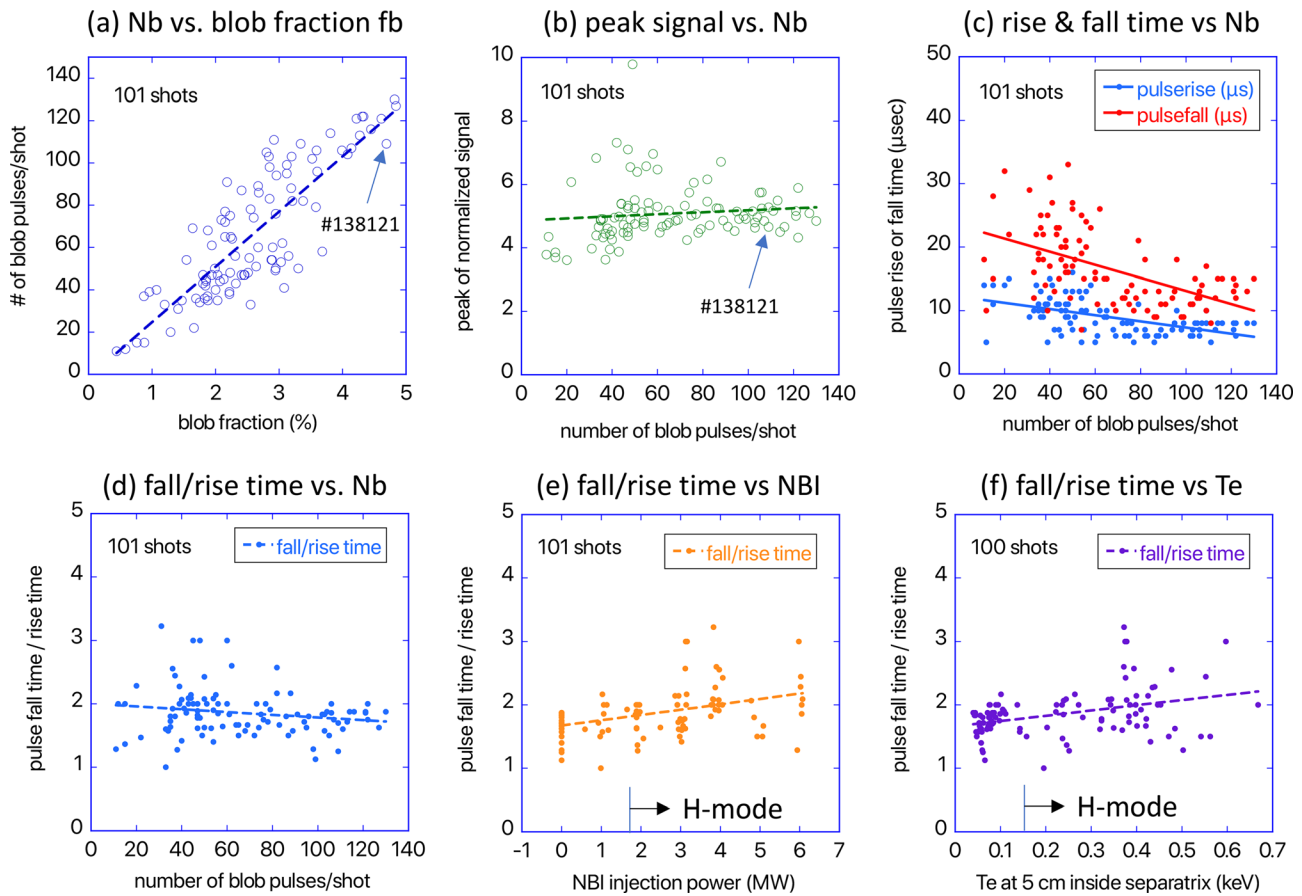


FIG. 3. Statistics of blob pulses from the 101-shot database. Part (a) shows the number of blob pulses per shot N_b vs the blob fraction f_b as defined in Ref. 1. Part (b) shows the average peak of the normalized blob amplitude vs N_b , and part (c) shows the rise and fall times of the best fits to the blob pulses for each shot vs N_b . The bottom row shows the ratio of the average blob pulse fall time over the rise time for each shot vs N_b in part (d), vs NBI power in part (e), and vs T_e at 5 cm inside the separatrix in part (f).

over the 7.5 cm just outside the separatrix over the same 10 ms times (but over a larger poloidal range of the images). It was shown in Ref. 1 that the blob fraction, defined there and here as the fraction of times the normalized GPI signal was above three in the SOL, was generally (but not always) larger for Ohmic plasmas than for H-mode plasmas.

Figure 3(a) shows that there is a high correlation coefficient of 0.84 between these two different measures of blob population N_b and f_b , which is not too surprising. For comparison, the cross-correlation magnitude expected for a similarly sized set of 100 data pairs chosen at random between (0, 1) is only 0.08, as found by averaging over 10 000 such data pair sets (see Ref. 1 for details). The probability of an accidental random correlation of these 100 pairs being ≥ 0.3 is only 0.2%, so the observed correlation of 0.84 of these 101 parameter pairs is very significant. The two shots with $N_b = 0$ (not shown) were quiescent H-modes which had very low $f_b = 0.12\%$ (No. 138614) and $f_b = 0.4\%$ (No. 138620).

Figure 3(b) shows a comparison between the number of blob pulses per shot N_b and the peak of the normalized blob amplitude, which was 4.7 for shot No. 138121 in Fig. 2(b). The range of these peak amplitudes for this database varied from 3.7 to 9.8; however, there was little or no systematic variation with the number of

blobs/shot N_b , with a correlation coefficient of 0.11. There was, of course, a considerable variation in the peak blob amplitudes vs time at any given radial position, as illustrated in Fig. 1.

Figure 3(c) shows the exponential blob pulse rise time and fall time for each shot in the database, including the rise and fall times of 10 and 17 μs for No. 138121 of Fig. 2(b). The rise times ranged from 5 to 16 μs with an average $\tau_r = 9.0 \pm 2.7 \mu\text{s}$, and the fall times ranged from 7 to 33 μs with an average of $\tau_f = 16.6 \pm 5.8 \mu\text{s}$. There was a somewhat surprising trend for decreasing rise and fall times with higher blob number N_b , as shown by the linear fits in this plot, with a correlation coefficient for both of -0.54 .

Figures 3(d)–3(f) show three parameter dependences of the ratio of the blob fall time to the blob rise time. The average blob fall time/rise time is 1.9 ± 0.4 with little or no dependence of the fall time/rise time on N_b , as shown in Fig. 3(d). The fall time/rise time increases slightly with NBI power, as shown in Fig. 3(e), where the H-mode threshold for these data is about 1.8 MW. Figure 3(f) shows that the fall/rise time ratio also increases slightly with the edge electron temperature T_e at 5 cm inside the separatrix, where H-mode is found when $T_e \geq 0.15 \text{ keV}$ at this radius (one shot is missing T_e data). Thus, the blob pulses are slightly more asymmetrical in H-mode than in Ohmic

plasmas. The correlation coefficients were -0.17 for (d), 0.42 for (e), and 0.36 for (f). The correlation coefficients in (d)–(f) do not increase significantly when the blob asymmetry parameter of the statistical model,¹⁰ namely (blob rise time/blob duration), was used instead of fall/rise time, i.e., these correlations were -0.13 vs N_b for (d), -0.40 vs NBI for (e), and -0.32 vs T_e for (f). The blob fall/rise time ratio also increases slightly with the plasma current, with a correlation coefficient of 0.32 . Note that the blob fall/rise time ratio is not expected to correlate with the SOL width but can be viewed as a basic physical parameter of these blobs.

In summary of results so far, the blob pulse shapes in the 101-shot database were well fit by an exponential rise and fall time with a total blob pulse duration (rise time + fall time) of $\tau_d = 25.5 \pm 8.2 \mu\text{s}$. Of course, the exact blob pulse duration also depends on the definition of the blob threshold, which, for this paper, is three times the time-average signal at each pixel. This blob definition selects relatively large blobs which are naturally less frequent than found for a lower blob threshold, as discussed in Ref. 1.

Another basic parameter in the statistical theories of blobs is the waiting time distribution between blobs. Figure 4(a) shows the blob waiting time distribution measured for the Ohmic shot used in Figs. 1 and 2 (No. 138121), in which the times between successive blob peaks were recorded for 10 ms periods for all of the six pixels of Fig. 2(a) within the range from 0 to 7.5 cm outside the separatrix. There were only 103 wait times measured for these 109 blobs since, for each separate radius, there is one blob at the end of the time series with no successor. The measured blob waiting times as shown in Fig. 4 have a broad distribution from 0.053 to 2.295 ms with a mean value of $532 \mu\text{s}$. The shortest wait time in Fig. 4 of $53 \mu\text{s}$ was previously shown in Fig. 1(a) at 225 ms, just above the $50 \mu\text{s}$ excluded time around each blob. This average of the measured waiting times is close to the average expected for a random set of $N_b = 109$ blobs over 10 ms at six different radii, i.e., $\tau_w = 6 \times 10 \text{ ms}/N_b = 550 \mu\text{s}$, as expected.

Figure 4(b) shows the waiting time distribution for all blobs in the 101-shot database, including all six radial locations for each shot. The time bins and waiting time range in Fig. 4(b) are the same as in Fig. 4(a) but have a total of 5595 wait times or ~ 55 per shot. The distribution in (b) is similar to that in (a), but (b) shows more clearly a near-exponential waiting time distribution with an e-folding time of ~ 0.590 ms between 0.375 and 2.5 ms for the database as a whole. This

broad distribution is consistent with random blob waiting times, such that the blob events are uncorrelated with each other as assumed in the Poisson process model of Ref. 2 and seen experimentally, for example, in Refs. 5 and 6.

Figure 5(a) shows the average blob pulse waiting time t_w calculated for every shot in the database using the simplified formula above $\tau_w \sim (60 \text{ ms}/N_b)$ and plotted vs the blob fraction for that shot [note Fig. 5(a) shows the inverse of Fig. 3(a)]. The shot-averaged waiting time was $\tau_w = 1.2 \pm 0.85$ ms, with a range from $\tau_w = 0.46$ to 5.45 ms corresponding to the range of N_b measured for these shots. The dashed curve is the best power law fit: $\tau_w(\text{ms}) = 2.5 f_b (\%)^{-1.01}$, which shows a trend for higher waiting times for lower blob fractions, as expected. The distribution of waiting times was broad like that in Figs. 1 and 4 for all shots in the database (shots with quasi-periodic MHD-induced blobs were excluded from the database in Ref. 1).

Figure 5(b) shows these waiting times vs the average blob durations τ_d for each shot, where τ_d is the sum of the exponential fit times for the average blob pulse rise and fall. These durations range from 12 to $46 \mu\text{s}$ (note the suppressed zero in this figure). The waiting times tend to increase slightly with the pulse duration, as shown by the linear fit. The six shots with waiting times ≥ 2 ms are all H-modes with very few blobs, for example, shot No. 141324 (as marked) with $\tau_w = 5$ ms, which was also highlighted in Ref. 1. These six shots with the highest τ_w do not have a consistent blob duration τ_d .

Figure 5(c) shows the blob intermittency parameter $\gamma_b = \tau_d/\tau_w$ vs f_b for the same 101 shots. This blob pulse intermittency varies from $\gamma_b = 0.3\%$ to 5.0% and increases nearly linearly with the blob fraction, with a high 0.89 correlation between the two. This is not too surprising since the blob pulse duration time is about the same as the time the signal spends above the threshold and a shorter waiting time implies both a larger blob intermittency and a larger blob fraction.

For the sake of simplicity, the results in Figs. 3–5 were averaged over the radial range of pixels from 0 to 7.5 cm outside the separatrix, as done in the previous paper on blob fractions.¹ Yet, there might be some radial profile dependence within this region, as can be seen in Fig. 2(a) and noted elsewhere,¹¹ so the temporal blob structure was also evaluated at three separate pixels at radii of 1.5, 4.5, and 7.5 cm outside the separatrix for the 101-shot database. The average number of blobs per shot decreased with an increasing radius over this range from $N_b = 17 \pm 13$ to 12 ± 6 to 7 ± 6 , as illustrated in Figs. 1 and 2(a)

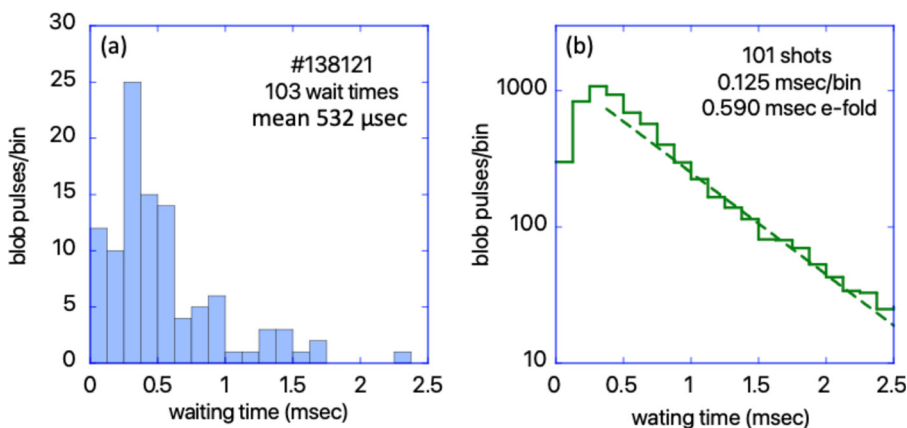


FIG. 4. In (a) is a histogram of the waiting time distribution for all blob pulses for all six radial locations for shot No. 138121, as in Fig. 2(a). The average waiting time is $532 \mu\text{s}$, with a wide range from 0.053 to 2.295 ms. There are only 103 waiting times in the 109 blobs for these six pixels. In (b) is a histogram of the wait time distribution for all 101 shots in the database for all six radial locations. The 5595 wait times in (b) show a near-exponential decay time of ~ 0.590 ms between 0.375 and 2.5 ms.

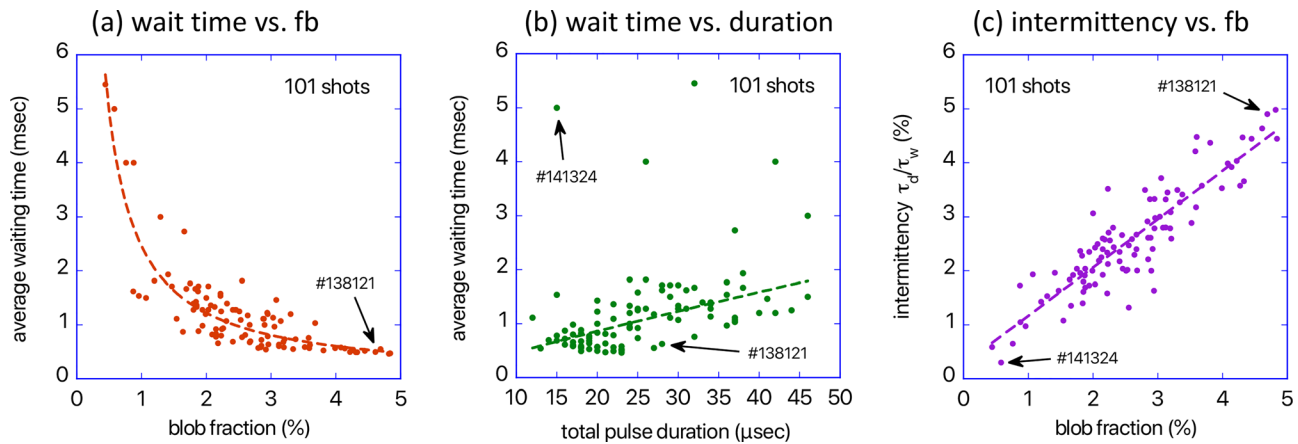


FIG. 5. Statistics of blob waiting times and total pulse widths from the 101-shot database. Part (a) shows the average blob pulse waiting time τ_w (defined as $\tau_w = 60 \text{ ms}/N_b$) vs the blob fraction f_b as defined in Ref. 1. Part (b) shows the waiting time τ_w vs the total pulse duration $\tau_d (= \tau_r + \tau_f)$, and part (c) shows the blob intermittency parameter $\gamma_b = \tau_d/\tau_w$ vs f_b for the same shots. The six shots with $\tau_w \geq 2 \text{ ms}$ are all H-mode shots with a relatively low blob fraction (like No. 141324).

for shot No. 138121. The average peak of the normalized blob amplitude over this same radial range increased slightly from 4.2 ± 0.8 to 5.6 ± 1.7 to 5.8 ± 3.0 , while the average blob width (above the threshold of three) increased from 9.7 ± 4.6 to $24.7 \pm 11.2 \mu\text{s}$ to 23.0 ± 13.0 (only peaks and widths for shots with at least one blob at that radius were used). However, since each of these results has a relatively large standard deviation (indicated by the error bars), these radial trends are only marginally significant when averaged over the entire database.

For the sake of completeness, the sensitivity of the blob pulse structures with respect to the blob threshold definition was also checked. The blob definition used above of three times the mean of the normalized signal was varied from two to four times the mean level. For shot No. 138121 used for Fig. 2, the number of blobs increased from $N_b = 109$ for a threshold of three times the mean to $N_b = 203$ for a threshold of two times the mean and decreased to $N_b = 56$ for a threshold of four times the mean. A similar variation in the number of blobs with respect to this threshold variation was shown in Fig. 5 of Ref. 1. Thus, the average blob waiting times decreased by about a factor of 2 for the lower threshold and increased by about a factor of 2 for the higher threshold since there are more blobs with a lower threshold. The average blob pulse height varied from 3.6 to 4.6 to 5.7 over the threshold variation of 2 to 3 to 4. However, the average blob rise times and fall times were very similar over this variation; namely, rise times of $\tau_r = 9, 10,$ and $9 \mu\text{s}$ for thresholds of two, three, and four, and fall times of $\tau_f = 16, 17,$ and $17 \mu\text{s}$ for thresholds of two, three, and four. When the alternative blob definition of 2.5 times the standard deviation above the mean was used at each pixel, these thresholds ranged from 2.6 to 3.4 times the mean, and so, the results were very similar to the three times the mean threshold, namely, with $N_b = 117$, peak height 4.5, and rise and fall times of 10 and $17 \mu\text{s}$.

III. SUMMARY AND DISCUSSION

These results on the time dependence of blobs in the SOL of NSTX can be summarized as follows:

- The time dependence of the blob pulse shapes was generally well fit by an exponential rise and fall, as illustrated in Fig. 2. Over the 101-shot database described in Ref. 1, there was a slight decrease in the blob rise and fall times with an increasing number of blobs/shot N_b , as shown in Fig. 3(c). The total blob pulse duration was $\tau_d = 25.5 \pm 8.2 \mu\text{s}$, and the ratio of the fall/rise times was 1.9 ± 0.4 , as shown in Figs. 3(d)–3(f).
- The waiting times of the blob pulses had a broad distribution within a single shot and over the whole 101-shot database, as illustrated in Fig. 4. This broad distribution is consistent with random uncorrelated blob waiting times as assumed in the Poisson process model of Ref. 2 and seen experimentally for example in Refs. 5 and 6. The averaged waiting times per shot ranged from $\tau_w = 0.46$ – 5.45 ms over the database, as shown in Fig. 5, and decreased with increasing blob fraction, as shown in Fig. 5(a). The blob intermittency parameter $\gamma_b = \tau_d/\tau_w$ ranged from $\gamma \sim 1\%$ – 5% for shots in this database and increased with the blob fraction, as shown in Fig. 5(c).

Although these results will now be compared with previous results from other machines, it should be emphasized that other experiments generally used different diagnostics and different blob definitions, so these comparisons are largely qualitative.

Blob pulse shapes were previously measured using conditional sampling of Langmuir probe signals in the SOL, as reviewed in Ref. 4, generally with a blob threshold of ≥ 2.5 times the RMS fluctuation level above average. For example, in TCV (Tokamak à Configuration Variable) there was a very steep blob pulse rise and much slower fall with a total pulse duration $\tau_d \sim 10$ – $25 \mu\text{s}$,¹² whereas the blob pulses were similar in duration but more symmetrical in time in DIII-D,³ TEXTOR,¹³ and NSTX.¹⁴ Average blob rise times and fall times in Alcator C-Mod were 5 and $15 \mu\text{s}$, respectively, with an average waiting time of $\sim 0.3 \text{ ms}$, so $\tau_d/\tau_w \sim 0.07$.¹⁵ Blob rise times of $11 \mu\text{s}$ and fall times of $19 \mu\text{s}$ were measured in KSTAR,¹⁶ similar to Fig. 2(b) here. The blob pulse duration increased monotonically with radius in the edge and SOL from 2.6 to $5.8 \mu\text{s}$ in the TCABR tokamak in Ref. 17,

and blob pulses durations in the duration range of 11–17 μs were found in the SOL of the COMPASS tokamak using lithium-beam emission spectroscopy.¹⁸

Blob waiting times in other devices generally had a broad and random distribution with $\tau_w \sim 0.1\text{--}1$ ms and $\gamma_b = \tau_d/\tau_w < 1$,^{4,13,15} qualitatively similar to the results found here. A recent measurement of ion flux to a wall-mounted Langmuir probe at the outer midplane in JET¹⁹ showed blobs with $\tau_d \sim 10\text{--}200$ μs , $\tau_w \sim 1\text{--}10$ ms, and $\tau_d/\tau_w \sim 0.3$.

In contrast to the studies above done using conditional averaging, the recent work of Kube *et al.*⁶ analyzed the entire probability distribution function of GPI fluctuations in the Alcator C-Mod SOL, including all small amplitude fluctuations in the probability distribution function. The calculated fluctuation intermittency parameter of $\gamma = 2\text{--}4$ reflected a significant temporal overlap of the entire spectrum of fluctuations analyzed this way when compared with the much smaller blob intermittency of $\gamma_b = 0.07$ for large blobs found using conditional sampling for similar C-Mod data,¹⁵ which is similar to results in the present paper.

The blob intermittency results in this paper are generally consistent with the assumptions of a statistical model for SOL blobs as developed in Ref. 2 and used in Ref. 1. As noted in the previous paragraph, the blob intermittency parameter $\gamma_b = \tau_d/\tau_w$ should not be confused with the fluctuation intermittency parameter $\gamma = \tau_d/\tau_{w0}$, i.e., including all fluctuations. Here, τ_{w0} is the average waiting time between pulses without invoking any threshold. In Ref. 1, we deduced γ by comparing the measured blob fraction f_b to the same parameter calculated from the statistical model which, following Ref. 2, assumed Poisson statistics for the pulse emission and an exponential distribution of pulse amplitudes. Not surprisingly, this procedure results in similar values for γ using the present dataset. For example, taking $f_b = 0.05$ and a threshold of three times the mean signal, the statistical model gives a root for the fluctuation intermittency parameter at $\gamma = 1.00$. The other extreme of the present dataset with $f_b \approx 0.01$ gives $\gamma = 2.5$. These order unity, or slightly larger, values of fluctuation intermittency are similar to those found in Ref. 1 and in other devices. A more detailed discussion of the relationship between f_b and γ is given in the Appendix.

In conclusion, the experimental results of this paper help clarify the temporal structure of blobs in the SOL of NSTX, which adds a new perspective to the previous analysis of the spatial structure and velocity of blobs in the SOL of NSTX.²⁰ However, these results do not directly address the practical issues of predicting the radial profiles of temperature and density in the SOL since GPI cannot be used to evaluate particle or heat transport. Instead, these results on the structure of blobs can help validate theoretical models of SOL turbulence, which could then be used to understand and predict the particle and heat transport in the SOL of future devices.

Theoretical understanding of the blob pulses in tokamaks has been developing for many years, as described in the review.⁴ An early model of the blob pulses in the context of self-organized criticality was presented for JET data in Ref. 21, and the statistical model of Garcia has been used in much recent work.^{5,6,11,12,15,16} Computational fluid and kinetic models for SOL turbulence have been improving rapidly, and generic predictions for blob pulse duration and waiting time such as in Ref. 22 look qualitatively similar to the results from NSTX in the present paper. It would be very interesting to perform such simulations for NSTX to make a direct quantitative comparison to the blob statistics in this paper.

ACKNOWLEDGMENTS

The authors thank R. J. Maqueda, B. Davis, and D.P. Stotler and J. L. Terry for collaboration on the GPI diagnostic over many years, and S. Banerjee, N. Bisai, A. Diallo, and D. A. Russell for discussions of blob physics and GPI, B. LeBlanc for the Thomson scattering data, S. Sabbagh for the EFIT results, and the NSTX/NSTX-Upgrade Team and management for their continued support of this work. This material is based upon the work supported by the USDOE Contract No. DE-AC02 09CH11466 and the Office of Fusion Energy Sciences Award No. DE-FG02-97ER54392.

AUTHOR DECLARATIONS

Conflict of Interest

The authors have no conflicts to disclose.

Author Contributions

Stewart J. Zweben: Conceptualization (equal), Data curation (equal), and Formal analysis (equal). **Mate Lampert:** Data curation (equal). **James R. Myra:** Data curation (equal) and Formal analysis (equal).

DATA AVAILABILITY

The data that support the findings of this study are openly available in the PPPL Dataspace Archive at <http://arks.princeton.edu/ark:/88435/dsp018p58pg29j>, Ref. 23, including sample videos of the GPI data.

APPENDIX: RELATIONSHIP OF THE BLOB FRACTION TO FLUCTUATION INTERMITTENCY

Recall that f_b is defined as the fraction of time the (GPI) signal remains above a given threshold T , where the signal is normalized to have a mean value of 1 and $T = 3$ is chosen. The fluctuation intermittency parameter is $\gamma = \tau_d/\tau_{w0}$, where τ_d is the pulse duration time and τ_{w0} is the mean waiting time between pulses of any amplitude, not just those above threshold.

A theoretical model of the statistics of blob pulses was developed in Ref. 2 and expanded upon in Ref. 24. Assuming an exponential pulse shape and exponentially distributed pulse amplitudes, the probability distribution function of fluctuation amplitudes of a signal s is given by a gamma distribution, i.e.,

$$P(s) = \frac{\gamma}{\langle s \rangle \Gamma(\gamma)} \left(\frac{\gamma s}{\langle s \rangle} \right)^{\gamma-1} \exp\left(-\frac{\gamma s}{\langle s \rangle}\right), \quad (\text{A1})$$

where $\langle s \rangle$ is the mean value of the signal and γ is the fluctuation intermittency parameter. With these assumptions, the blob fraction is given by

$$f_b = \int_T^{\infty} ds P(s). \quad (\text{A2})$$

A plot of f_b vs γ for different thresholds is shown in the upper panel of Fig. 6. There are two (or no) solutions for γ for a given value of f_b and T . For the experimental threshold level of $T = 3$ (blue curve) and $f_b \approx 0.05$, the lower root is $\gamma = 0.024$ and the upper root is $\gamma = 1.00$.

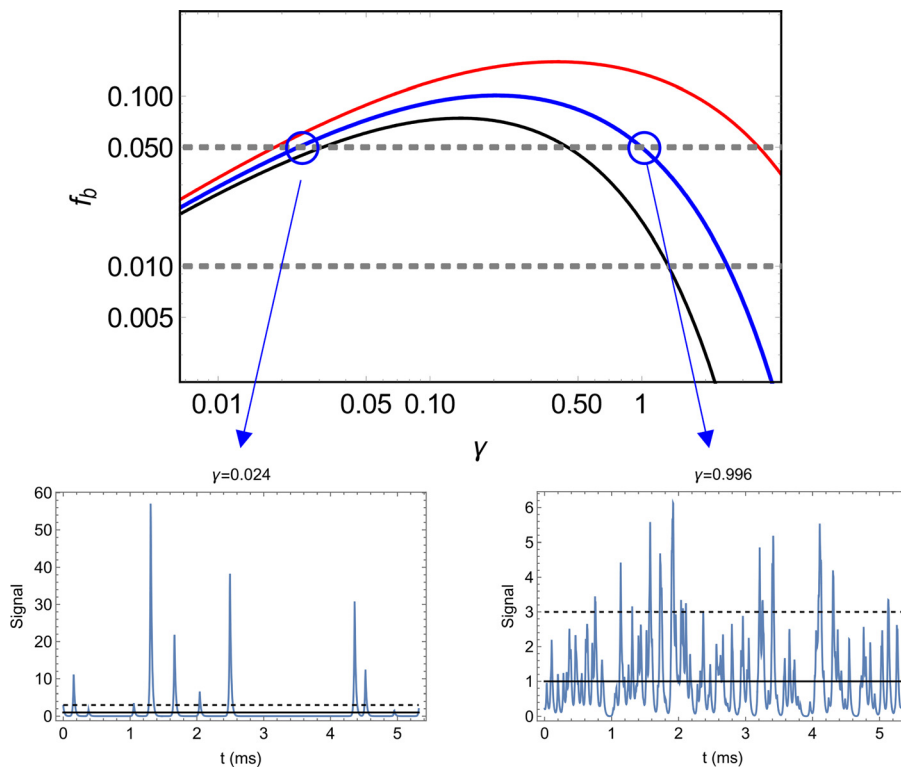


FIG. 6. Upper panel: variation of blob fraction with fluctuation intermittency parameter for three different threshold values: $T=2$ (red), 3 (blue), and 4 (black). The dashed lines demarcate the range of f_b values observed in the GPI data. Lower panels: results of statistical simulations for the normalized signal $s(t)$ using experimental parameters and taking $\gamma=0.024$ (left) and $\gamma=1.00$ (right). The dashed lines indicate the threshold level, where $s=3$ and the solid line is the mean signal level $s=1$.

The lower panels show the results of two statistical simulations for these values of γ . The simulations randomly superimposed exponential pulses with parameters chosen to model the GPI experimental conditions: $\tau_r=10 \mu\text{s}$, $\tau_f=17 \mu\text{s}$, and mean waiting time for blobs above threshold $\tau_w=532 \mu\text{s}$. The actual random time between pulses obeyed Poisson statistics, and the pulse amplitude distribution was exponential. The simulated time histories were sampled every $2.5 \mu\text{s}$ corresponding to the GPI time resolution. The results for the total signal were then normalized to have a mean value of 1, like the experimental data.

The lower branch has little activity at small signal levels, and the peak signal levels are very large: since the pulses are infrequent, large amplitudes result when $\langle s \rangle$ is normalized to 1. In contrast, the upper branch has many fluctuations below the threshold and a much smaller peak signal level. The number of events that exceed the threshold is similar, within statistical fluctuations, for the two cases as guaranteed by construction.

These figures are to be compared with Fig. 1. Both from the qualitative features of the fluctuating signal and the scale of the peak amplitudes, it is clear that the upper branch provides the best model of the full signal. Thus, f_b measures a very different quantity than γ , but γ can be deduced from a measurement of f_b if a statistical model of all the fluctuations is used to make this connection.

REFERENCES

- ¹S. J. Zweben, S. Banerjee, N. Bisai, A. Diallo, M. Lampert, B. LeBlanc, J. R. Myra, and D. A. Russell, *Phys. Plasmas* **29**, 012505 (2022).
- ²O. E. Garcia, *Phys. Rev. Lett.* **108**, 265001 (2012).
- ³J. A. Boedo, D. L. Rudakov, R. A. Moyer, G. R. McKee, R. J. Colchin, M. J. Schaffer, P. G. Stangeby, W. P. West, S. L. Allen, T. E. Evans, R. J. Fonck, E. M. Hollmann, S. Krasheninnikov, A. W. Leonard, W. Nevins, M. A. Mahdavi, G. D. Porter, G. R. Tynan, D. G. Whyte, and X. Xu, *Phys. Plasmas* **10**, 1670 (2003).
- ⁴D. A. D'Ippolito, J. R. Myra, and S. J. Zweben, *Phys. Plasmas* **18**, 060501 (2011).
- ⁵A. Theodorsen, O. E. Garcia, R. Kube, B. LaBombard, and J. L. Terry, *Phys. Plasmas* **25**, 122309 (2018).
- ⁶R. Kube, A. Theodorsen, O. E. Garcia, D. Brunner, B. LaBombard, and J. L. Terry, *J. Plasma Phys.* **86**, 905860519 (2020).
- ⁷F. Militello and J. T. Omotani, *Nucl. Fusion* **56**, 104004 (2016).
- ⁸N. R. Walkden, A. Wynn, F. Militello, B. Lipschultz, G. Matthews, C. Guillemaut, J. Harrison, D. Moulton, and JET Contributors, *Plasma Phys. Controlled Fusion* **57**, 085009 (2017).
- ⁹S. J. Zweben, J. L. Terry, D. P. Stotler, and R. J. Maqueda, *Rev. Sci. Instrum.* **88**, 041101 (2017).
- ¹⁰O. E. Garcia and A. Theodorsen, *Phys. Plasmas* **24**, 032309 (2017).
- ¹¹A. Theodorsen, O. E. Garcia, R. Kube, B. LaBombard, and J. L. Terry, *Nucl. Fusion* **57**, 114004 (2017).
- ¹²O. E. Garcia, J. Horacek, R. A. Pitts, A. H. Nielsen, W. Fundamenski, V. Naulin, and J. J. Rasmussen, *Nucl. Fusion* **47**, 667 (2007).
- ¹³Y. H. Xu, S. Jachmich, R. R. Weynant, and TEXTOR Team, *Plasma Phys. Controlled Fusion* **47**, 1841 (2005).
- ¹⁴J. A. Boedo, J. R. Myra, S. J. Zweben, S. Maingir, R. J. Maqueda, V. A. Soukhanovskii, J. Ahn, J. W. Canik, N. Crocker, D. A. D'Ippolito, R. Bell, H. Kugel, B. Leblanc, L. A. Roquemore, D. L. Rudakov, and NSTX Team, *Phys. Plasmas* **21**, 042309 (2014).
- ¹⁵O. E. Garcia, R. Kube, A. Theodorsen, B. LaBombard, and J. L. Terry, *Phys. Plasmas* **25**, 056103 (2018).
- ¹⁶O. E. Garcia, R. Kube, A. Theodorsen, J.-G. Bak, S.-H. Hong, H.-S. Kim, KSTAR Project Team, and R. A. Pitts, *Nucl. Mater. Energy* **12**, 36 (2017).
- ¹⁷M. Zurita, W. A. Hernandez, C. Crepaldi, F. A. C. Pereira, and Z. O. Guimaraes-Filho, *Phys. Plasmas* **29**, 052303 (2022).

- ¹⁸A. Bencze, M. Berta, A. Buzaś, P. Hacek, J. Krbec, M. Szutyányi, and COMPASS Team, *Plasma Phys. Controlled Fusion* **61**, 085014 (2019).
- ¹⁹N. R. Walkden, A. Wynn, F. Militello, B. Lipschultz, G. Matthews, C. Guillemaut, J. Harrison, D. Moulton, and JET Contributors, *Nucl. Fusion* **57**, 036016 (2017).
- ²⁰S. J. Zweben, W. M. Davis, S. M. Kaye, J. R. Myra, R. E. Bell, B. P. LeBlanc, R. J. Maqueda, T. Munsat, S. A. Sabbagh, Y. Sechrest, D. P. Stotler, and NSTX Team, *Nucl. Fusion* **55**, 093035 (2015).
- ²¹R. Sanchez, B. Ph. van Milligen, D. E. Newman, and B. A. Carreras, *Phys. Rev. Lett.* **90**, 185005 (2003).
- ²²G. Decristoforo, A. Theodorsen, J. Omotani, T. Nicholas, and O. E. Garcia, *Phys. Plasmas* **28**, 072301 (2021).
- ²³S. J. Zweben, M. Lampert, and J. R. Myra, see <http://arks.princeton.edu/ark:/88435/dsp018p58pg29> for “Temporal Structure of Blobs in NSTX, PPPL Dataspace Archive” (2022)
- ²⁴A. Theodorsen and O. E. Garcia, *Phys. Plasmas* **23**, 040702 (2016).